Geophys. J. Int. (2004) doi: 10.1111/j.1365-246X.2004.02235.x

Probability density functions for radial anisotropy from fundamental mode surface wave data and the Neighbourhood Algorithm

Caroline Beghein and Jeannot Trampert

Department of Earth Sciences, Utrecht University, Budapestlaan 4, PO Box 80021, *Utrecht* 3508 TA, *the Netherlands. E-mail: beghein@geo.uu.nl*

Accepted 2004 January 14. Received 2003 December 22; in original form 2003 May 15

SUMMARY

We applied Sambridge's Neighbourhood Algorithm (NA) to degree-8 fundamental mode Love and Rayleigh wave phase velocity maps between 40 and 150 s to find models of radial anisotropy in the upper 220 km of the mantle. The NA is a powerful tool to explore a multidimensional model space and retrieve an ensemble of models from which statistical inferences (posterior probability density functions (PPDFs) and trade-offs) can be made. We sought solutions for density anomalies and perturbations in the five elastic coefficients that describe transverse isotropy and obtained independent probability density functions for *S*-wave anisotropy, *P*-wave anisotropy, intermediate parameter η, V_p, V_s and density anomalies. We find robust departures from PREM in *S*-wave anisotropy (ξ) under cratons and oceans alike, with a clear change of sign in the anomalies with respect to the reference model at approximately 100 km depth. No significant difference is observed between cratons and oceans, both in the amplitude and depth variation of ξ. The signal within continents is clearly age related, with platforms and tectonically active regions characterized by a rapid decrease in ξ with depth, while cratons display a more constant signal. A similar age dependence in *S*-wave anisotropy is also observed beneath oceans: a strong and rapidly decreasing anisotropy for young oceans and a more constant anisotropy for older oceans. Perturbations in *P*-wave anisotropy (ϕ) are small and limited to the shallowest part of the continents. A small age-dependent signal for ϕ is observed beneath oceans. Anomalies in intermediate parameter η are similar to those in ϕ (but not globally correlated), but the deviation from PREM is stronger for η than for ϕ. Cratons appear to be devoid of any η anisotropy in the top 100 km. There is no obvious global correlation between deviations in ϕ and deviations in ξ, and the ratio between $d\eta$ and $d\xi$ is clearly regionally variable, which cautions against the use of commonly used proportionality factors between these variables in inversions. In all regions, we found a good correlation between the equivalent isotropic *P*- and *S*-wave velocity anomalies, with a ratio $d\ \ln V_s/d\ \ln V_p$ close to 1. Density anomalies were not sufficiently well resolved with fundamental mode data alone, but do not influence the results for anisotropy.

Key words: full model space search, mantle, radial anisotropy, surface waves.

1 INTRODUCTION

Upper-mantle seismic anisotropy can be observed using different kinds of seismological data: body waves, normal modes and surface waves. Direct observations of anisotropy are provided by body waves through shear wave birefringence and through the azimuthal dependence of propagation of P_n waves, first observed by Hess (1964) in the Pacific ocean. The dispersion of surface waves can also be used to study azimuthal anisotropy (Forsyth 1975), but it also provides information on radial anisotropy. Radial anisotropy, or polarization anisotropy, describes the anisotropic behaviour of a cylindrically symmetric medium whose symmetry axis is in the radial direction. Its observation is not direct. It was first introduced by Anderson (1961) to explain the incompatibility between isotropic Rayleigh and Love phase velocity maps, known as the Love–Rayleigh discrepancy. There is now a general agreement that anisotropy is the result of the preferred alignement of olivine crystals, a highly anisotropic mineral very abundant in the upper mantle, possibly oriented by a plastic flow in the oceans (Tanimoto & Anderson 1984) and orogenic deformation in continents (Silver & Chan 1991).

It is clear that surface waves require the uppermost mantle to be radially anisotropic on average (e.g. PREM Dziewonski & Anderson 1981), but lateral variations are found in many studies. Oceanic regions appear highly anisotropic as shown by Lévêque *et al.* (1998) for the Indian ocean, by Silveira & Stutzmann (2002) for the Atlantic ocean and by Lévêque & Cara (1983), Nataf *et al.*

(1984), Montagner (1985, 2002), Nishimura & Forsyth (1989), Montagner & Nataf (1988) and Ekström & Dziewonski (1998) for the Pacific ocean. Radial anisotropy under continents was also observed for Africa (Hadiouche *et al.* 1989), North America (Cara *et al.* 1980), Australia (Debayle & Kennett 2000) and Western Europe (Lévêque & Cara 1983). A global study (Montagner & Tanimoto 1991), based on the inversion of surface wave data, showed an upper-mantle anisotropy more pronounced beneath oceans than beneath continents. In a simultaneous waveform inversion of surface waves, overtones and body waves, Gung *et al.* (2003) recently confirmed the existence of anomalous radial anisotropy under the Pacific ocean, as observed by Ekström & Dziewonski (1998), but also showed significant variations of anisotropy under the Indian ocean and under most continents. This seems to indicate that deviations of upper-mantle anisotropy from PREM are not specific to the Pacific ocean, as previously claimed (Ekström & Dziewonski 1998). The precise depth extent of anisotropy is still not fully clear, although its amplitude appears to decrease with depth. Differences among the various studies could simply arise from different resolutions and different inversion schemes. On the other hand, the strength of anisotropy could vary both laterally and with depth and could be a signature of the depth extent of continental roots (Gaherty & Jordan 1995; Gung *et al.* 2003).

The robustness of these models is difficult to assess. Some result from the difference between two tomographic models, obtained from separate inversions (e.g. Ekström & Dziewonski 1998). As explained by Lévêque & Cara (1983), separate inversions generally provide models that average the properties of the Earth in different ways (with different resolution kernels). It could therefore be quite dangerous to make inferences about the anisotropic properties of the Earth simply by substracting two models. Problems also arise in inversions made simultaneously for several parameters. It is well known that seismological inverse problems are generally non-unique, which means that the model parameters cannot be uniquely determined by observations. Imposing a regularization is a way to reduce the ensemble of possible solutions, or to choose a particular solution among all the models compatible with the data. However, this introduces many hidden problems that can make both the interpretation and the uncertainty assessment of tomographic models less straightforward than usually assumed (Trampert 1998). Several levels of regularization are involved when solving inverse problems. The physical variables used to describe the Earth are, strictly speaking, continuous functions of position and should be expanded in a complete set of basis functions. The choice of these basis functions should not matter as long as the expansion is complete. However, for practical reasons, they have to be truncated and this implies some level of regularization. More implicit regularization is introduced through the choice of the cost function that is minimized to find a solution (e.g. a χ^2 misfit and/or a model norm term). A general form of the cost function is (Tarantola 1987):

$$C_\lambda = \Delta_{\mathcal{D}}(\mathbf{d}, \mathbf{Am}) + \lambda \Delta_{\mathcal{M}}(\mathbf{m}, \mathbf{m}_0), \tag{1}$$

where $\Delta_{\mathcal{D}}$ and $\Delta_{\mathcal{M}}$ are measures of the distance between observation **d** and prediction **Am** in the data space and between the solution **m** and a reference model $\mathbf{m}_0$ in the model space, respectively. The choice of these norms is arbitrary and is some kind of *a priori* information. Common examples are:

$$\Delta_{\mathcal{D}}(\mathbf{d}, \mathbf{Am}) = (\mathbf{d} - \mathbf{Am})^\dagger \mathbf{C}_d^{-1} (\mathbf{d} - \mathbf{Am}) \tag{2}$$

and

$$\Delta_{\mathcal{M}}(\mathbf{m}, \mathbf{m}_0) = (\mathbf{m} - \mathbf{m}_0)^\dagger \mathbf{C}_m^{-1} (\mathbf{m} - \mathbf{m}_0). \tag{3}$$

$\dagger$ stands for the transpose of a matrix. $\mathbf{C}_d$ and $\mathbf{C}_m$ are data and model covariance operators, respectively, and $\mathbf{m}_0$ is a reference model. By minimizing the cost function, one simultaneously tries to optimize the data fit and some information in the model space (norm, smoothness). A compromise between these two properties is reached by choosing an arbitrary value for the trade-off parameter λ. The data covariance matrix $\mathbf{C}_d$ is often reduced to a diagonal matrix containing estimates of data uncertainties. The model covariance matrix $\mathbf{C}_m$ should be chosen using independent prior information on the model space (Tarantola 1987). The choice of λ, $\mathbf{C}_d$, $\mathbf{C}_m$ and the reference model $\mathbf{m}_0$ are explicit regularization on both the model space and the data space. Many levels of regularizations are thus implicitly and explicitly introduced when solving an inverse problem. It is, therefore, easily understandable that the resulting model could be dominated by such prior information.

Despite the choice of a model parametrization (basis functions), norms and data errors, the solution of seismological inverse problems is still highly non-unique. This is why additional constraints (explicit regularization λ and $\mathbf{C}_m$) on the model parameters need to be introduced. In studies of lateral variations of mantle anisotropy from surface wave data, only two (*S*-wave related) parameters can be resolved reasonably well from inversions. Two approaches are then usually taken to reduce the number of parameters: introducing scalings between the different unknowns or neglecting the parameters whose partial derivatives have the smallest amplitude. The first approach (e.g. Gung *et al.* 2003; Montagner & Tanimoto 1991) makes use of petrological considerations (Montagner & Anderson 1989) to choose the scalings between the parameters describing seismic anisotropy. However, the ratios between these parameters vary among the different studies (Nataf *et al.* 1986; Montagner & Tanimoto 1991). Authors also often introduce the assumption that thermal effects are dominant in the mantle by imposing a (positive) scaling between density and equivalent isotropic velocity perturbations. In the second approach (Montagner 1985; Montagner & Nataf 1988; Montagner 2002; Silveira & Stutzmann 2002), some model parameters are not taken into account, which introduces errors in the amplitude of the models recovered, but might also have other effects, more difficult to see. These assumptions can, for instance, restrict the solution to a certain class of models and rule out other solutions *a priori*.

Direct search approaches offer a way to obtain robust information on the properties of the Earth without having to introduce explicit *a priori* information on the model parameters (i.e. $\lambda = 0$ and eq. (3) is not used) for a given parametrization. The Neighbourhood Algorithm (NA) (Sambridge 1999a,b), an efficient model space search technique, was recently applied to tomographic problems to search for low-degree isotropic mantle models of *P*-wave and *S*-wave velocities (Beghein *et al.* 2002), and to seek perturbations in V_p, V_s and density (Resovsky & Trampert 2003). With this algorithm, all the models compatible with a given data set are found and robust probabilistic information on the model parameters (posterior probability density functions (PPDFs) and trade-offs) are obtained. The NA was also successfully employed to study inner-core anisotropy with normal mode data (Beghein & Trampert 2003) where it produced solutions previously unknown from traditional inversions and the models obtained were compatible with all independent body wave observations. Here, we applied the NA to the isotropic part of azimuthally anisotropic phase velocity maps for fundamental Love and Rayleigh modes (Trampert & Woodhouse 2003) to find models of radial anisotropy in upper mantle of the Earth. In order to obtain independent probability density functions (or likelihoods) for the different anisotropic parameters, we did not assume any scaling between the variables or neglect parameters whose sensitivity kernels have small amplitudes. These independent likelihoods can be compared and the relative behaviour of ξ, ϕ and η can be used to gain important information on the interior of the Earth. This research was, first and foremost, aimed to determine whether lateral variations of upper-mantle anisotropy are constrained by the data and are statistically robust. In addition, we could verify whether seismological data are compatible with traditional scalings between model parameters.

2 DATA AND PARAMETRIZATION

The data set was composed of the isotropic part of fundamental mode Rayleigh and Love wave phase velocity maps at 40, 50, 60, 70, 80, 90, 100, 115, 130 and 150 s (Trampert & Woodhouse 2003), corrected for the crustal model of Mooney *et al.* (1998). These phase velocity models were developed on a spherical harmonic (SH) basis up to degree 40. A local perturbation $\delta c/c(\theta, \phi)$ in the phase velocity, with respect to a spherically symmetric reference model, is given by a depth average of perturbations in the structure of the Earth (e.g. Dahlen & Tromp 1998):

$$ {}_k\left(\frac{\delta c}{c}\right)(\theta, \phi) = \int_0^a \delta\mathbf{m}(r, \theta, \phi)\,{}_k\mathbf{K}(r) r^2\, dr, \tag{4}$$

where a is the radius of the Earth, (θ, ϕ) is a point at the surface of the Earth and ${}_k\mathbf{K}(r)$ is the partial derivative for model parameter $\mathbf{m}(r)$, also called the sensitivity kernel. k discriminates between different surface wave frequencies. Both the phase velocity maps and the perturbations of the model parameters are developed on an SH basis (Edmonds 1960):

$$ {}_k\left(\frac{\delta c}{c}\right)(\theta, \phi) = \sum_{s=0}^{s_{\max}} \sum_{t=-s}^{s} {}_k\left(\frac{\delta c}{c}\right)_s^t Y_s^t(\theta, \phi), \tag{5}$$

$$ \delta\mathbf{m}(r, \theta, \phi) = \sum_{s=0}^{s_{\max}} \sum_{t=-s}^{s} \delta\mathbf{m}_s^t(r) Y_s^t(\theta, \phi) \tag{6}$$

and therefore

$$ {}_k\left(\frac{\delta c}{c}\right)_s^t = \int_0^a \delta\mathbf{m}_s^t(r)\,{}_k\mathbf{K}(r) r^2 dr. \tag{7}$$

We used degrees 0 to 8 only, because the derivative damping chosen by Trampert & Woodhouse (2003) hardly affects the lower degrees, which can be regarded as unbiased.

To determine the fit of a model to the data, we decided to use a χ^2 misfit (eq. 2), which measures the average data misfit compared to the size of the error bar. Although degrees 0 to 8 can be regarded as unbiased, an estimate of uncertainties on the phase velocities is needed. The same approach as in Beghein *et al.* (2002) was used here. Models from different studies were employed for periods of 40, 60, 80, 100 and 150 s: Wong (1989), Trampert & Woodhouse (1995, 1996, 2001, 2003), Laske & Masters (1996), Ekström *et al.* (1997) and van Heijst & Woodhouse (1999). At each selected period, a standard deviation was estimated for each SH coefficient. By analogy to error bars determined for normal mode structure coefficients (Resovsky & Ritzwoller 1998), we decided to assign averaged uncertainties to ${}_k(\frac{\delta c}{c})_s^t$, independent of the azimuthal order t and defined by:

$$ {}_k\sigma_s{}^2 = \frac{1}{2s+1} \sum_{t=-s}^{s} {}_k\sigma_s^{t\,2}, \tag{8}$$

where s is the degree of the SH and ${}_k\sigma_s^{t\,2}$ is the variance estimated for one particular SH coefficient. This should account for different measuring techniques of phase velocity, different data coverage and different regularization schemes in the construction of the maps between 40 and 150 s. At intermediate periods, we made a simple interpolation of the uncertainties obtained at 40, 60, 80, 100 and 150 s. We assumed, for convenience, that the errors were Gaussian distributed, but there were too few models to test this hypothesis.

An anisotropic medium with hexagonal symmetry is characterized by five independent elastic coefficients A, C, N, L and F, in the notation of Love (1927). Radial anisotropy occurs when the symmetry axis points in the radial direction and in seismology the following five parameters are often used: $\phi = 1 - C/A$, $\xi = 1 - N/L$, $\eta = 1 - F/(A - 2L)$ and one P and one S velocity. Note that the definitions of the first three parameters vary from author to author. The elastic coefficients are related to the wave speed of P waves travelling either vertically ($V_{\mathrm{PV}} = \sqrt{C/\rho}$) or horizontally ($V_{\mathrm{PH}} = \sqrt{A/\rho}$) and to the wave speed of vertically or horizontally polarized S waves ($V_{\mathrm{SV}} = \sqrt{L/\rho}$ or $V_{\mathrm{SH}} = \sqrt{N/\rho}$, respectively). Thus, ϕ describes P-wave anisotropy and ξ describes S-wave anisotropy. Parameter η describes the anisotropy of waves travelling with an intermediate incidence angle. In the convention used here, if there is no anisotropy ξ, ϕ and η are zero. Negative values of ξ correspond to $V_{\mathrm{SH}} > V_{\mathrm{SV}}$ and positive values of ϕ correspond to $V_{\mathrm{PH}} > V_{\mathrm{PV}}$. As an example, $\xi = -0.1$ means that horizontally polarized shear waves travel 10 per cent faster than vertically polarized shear waves.

We parametrized the models as perturbations of the Love parameters and perturbations of density with respect to PREM (Dziewonski & Anderson 1981). The corresponding sensitivity kernels are given in Mochizuki (1986), Tanimoto (1986) or Dahlen & Tromp (1998). The model parameters are expanded on an SH basis, as in eq. (6). The relation between the data and the structure of the Earth is then:

$$ \begin{aligned} {}_k\left(\frac{\delta c}{c}\right)_s^t = \int_{r_{\mathrm{cmb}}}^{a} \big[& {}_kK_A(r)\delta A_s^t(r) + {}_kK_C(r)\delta C_s^t(r) \\ & + {}_kK_N(r)\delta N_s^t(r) + {}_kK_L(r)\delta L_s^t(r) \\ & + {}_kK_F(r)\delta F_s^t(r) + {}_kK_\rho(r)\delta\rho_s^t(r)\big] r^2 dr, \end{aligned} \tag{9}$$

where r_{cmb} is the radius of the core–mantle boundary and a is the radius of the Earth. The problem thus naturally separates into individual SH components. We could have chosen to work in terms of velocity perturbations δV_{PV}, δV_{PH}, δV_{SH}, δV_{SV} instead of A, C, N and L, or in terms of $\delta\phi$, δV_{PV}, $\delta\xi$, δV_{SV} and $\delta\eta$, but this choice does not matter when using the NA, because the entire model space is explored and all the models compatible with the data are represented in the end. In case of an inversion, if no special care is taken, different parametrizations can lead to inconsistent results (Lévêque & Cara 1983; Tarantola 1987). With the NA, any information on the trade-offs among the model parameters, which changes the results of a classical linear inversion, is directly available through correlation matrices and 2-D posterior probability functions, as described by Sambridge (1999a,b). Examples specific to long wavelength tomography can also be found in Resovsky & Trampert (2002) and Beghein *et al.* (2002).

One of the great advantages of the method employed here is that we do not have to neglect or scale perturbations in the parameters to which the data are the least sensitive. Thus, no relation was assumed between $\delta\rho$ and equivalent isotropic shear wave velocity perturbations, or between $\delta\phi$, $\delta\xi$ and $\delta\eta$. We further did not use any explicit regularization in the model space via the cost function [no $\Delta_{\mathcal{M}}(\mathbf{m}, \mathbf{m}_0)$ term in eq. (1)]. Because the size of the model space that can be surveyed with the NA is limited and because we did not want to neglect parameters or impose any scaling between the different anisotropic parameters, we decided to reduce the number of unknowns by employing a rather coarse parametrization, with three layers delimited by 24 and 100 km depth, 100 and 220 km depth and 220 and 670 km depth. The choice of this layered division was not based on the depth resolution of the data, but was mainly motivated by computational resources. Still, our parametrization is sufficient to analyse the robustness of the anisotropic signal. We carefully tested that a coarse layering returns the representative averages of finer layers. This is because we get all models compatible with the data and thus no bias occurs because of the chosen parametrization. We prefer retrieving meaningful average values in coarse layers rather than putting unchecked constraints, such as scalings, on model parameters. A detailed geodynamical interpretation will clearly need a more refined analysis. Earlier studies showed that upper-mantle radial anisotropy decreases rapidly with depth and the sensitivity of fundamental mode surface waves at depths larger than 220 km is relatively small. The deepest layer was thus assumed to be isotropic. This is a strong assumption, but the correlation matrices obtained from the NA showed *a posteriori* that it did not have a large effect on the solution at depths shallower than 220 km (there were very little trade-offs among the different model parameters). We finally had a total of 15 model parameters.

A 5 per cent deviation for the elastic coefficients and a 2 per cent deviation for density were allowed from PREM. The choice of these boundaries is arbitrary and constitutes, together with the layered parametrization and the assumption of isotropy in the deepest layer, the only prior information introduced in the model space. However, because the problem is linearized, we have to stay within the framework of perturbation theory, which implies that perturbations in the model parameters should not be too large. On the other hand, we do not want these perturbations to be too small, because it would exclude possible good models. This is a trial and error part of the algorithm where the stability of results needs to be checked by changing the boundaries.

3 METHOD

Sambridge's NA (Sambridge 1999a,b) was employed to identify the regions of the model space that best fit the data. The NA explores the whole model space (within selected boundaries), including the null-space, and provides information on its approximate topology, that is, it identifies regions of relatively low and relatively high misfit, associated with high and low likelihoods, respectively. It differs from traditional inversion techniques by giving a view on all the models compatible with the data rather than choosing one by some subjective regularization. It differs from usual direct search approaches by characterizing the whole range of models contained in the model space instead of searching for one best solution by optimization of a cost function. The NA explores the model space by sampling different regions, similar to other direct search approaches. It also gives PPDFS for all model parameters, as explained below. The departure of these PPDFs from a Gaussian distribution can be used as a diagnostic of the degree of ill-posedness of the problem. The main advantage of mapping the complete model space concerns error analysis. Most linearized inversions give, by construction, a posterior model covariance smaller or equal to the prior covariance by construction (Tarantola 1987). If the cost function to be minimized has a large valley, that is if there is a large model null space, the posterior covariance can be seriously underestimated, depending on the prior covariance (Trampert 1998). We consider the width of the valley in the cost function as a realistic representation of the error bars in the absence of true physical prior information.

The NA is a two-stage procedure. The first stage consists of an efficient survey of the model space to identify the good data-fitting regions. It makes use of a geometrical construct, the Voronoi cells, to drive the search towards the best data-fitting regions while continuing to sample a relatively wide variety of different models. The use of the Voronoi cells makes this algorithm self-adaptive: with a good choice of some tuning parameters, one can explore the complete model space and there is always a possibility to escape from a local minimum. It also has the advantage of being able to sample several promising regions simultaneously. During this survey, the sampling density increases in the surroundings of the good models without losing information on the models previously generated (even the bad ones). The distribution of misfit obtained in the first stage is used to approximate the real PPDF. An importance sampling of this distribution is then performed in the second stage of the NA to generate a resampled ensemble that follows the approximate PPDF. This resampled ensemble is then integrated numerically to compute the likelihood associated with each model parameter (also called 1-D marginals), the covariance matrix and 2-D marginal PPDFs. The 2-D marginals can be used to infer the trade-offs between two variables. The same information can be deduced from the correlation matrix if a Gaussian approximation of the model space can be made. The likelihoods obtained for the various model parameters give a powerful tool to estimate true resolution and uncertainties, because they characterize the entire ensemble of models compatible with the data.

Each stage of the NA requires the tuning of parameters whose optimum values have to be found by trial and error. Their influence on the survey of the model space and on the Bayesian interpretation of the results was described by Sambridge (1999a,b) in general and by Resovsky & Trampert (2002) in a normal mode problem. To broaden the survey as much as possible, the two tuning parameters required for the first stage of the algorithm were kept equal. These two parameters are n_s, the total number of new models generated at each iteration, and n_r, the number of best data-fitting cells in which the new models are created. The advantage of using phase velocity maps is that the inverse problem is easily separable into SHs and the NA can solve individual inverse problems for each SH coefficient. Here, the NA was applied to each SH coefficient of the selected phase velocity maps up to degree 8 (81 coefficients). We increased the two parameters until the result was stable. We finally took $n_s = n_r = 100$ and the number of iterations varied between 300 and 700, depending on the SH coefficient treated. For the second stage of the NA, a few random walks of approximately 6000 steps were enough to insure the convergence of the integrals. In total, solving the problem for one SH coefficient took approximately one day on a SUN Ultrasparc (400 MHz).

The application of the NA to each SH component of the phase velocity maps provided PPDFs associated to each SH component $\delta m^t{}_s$ of the model parameters: δA^t_s, δC^t_s, δN^t_s, δL^t_s, δF^t_s and $\delta \rho^t_s$ in the top layers, and δA^t_s, δN^t_s and $\delta \rho^t_s$ in the third layer. Random values of these $\delta m^t{}_s$ were generated, according to their exact PPDF, to get probability density functions of the parameters of interest at each point in the Earth. Although we prefer working with A, C, N, L and F, seismologists prefer interpreting the variables ξ, ϕ and η. As explained above, as long as we look at all models compatible with the data, this choice is of no consequence. Rather than representing the thousands of tomographic models created, we decided to look at them from a statistical point of view. Histograms were

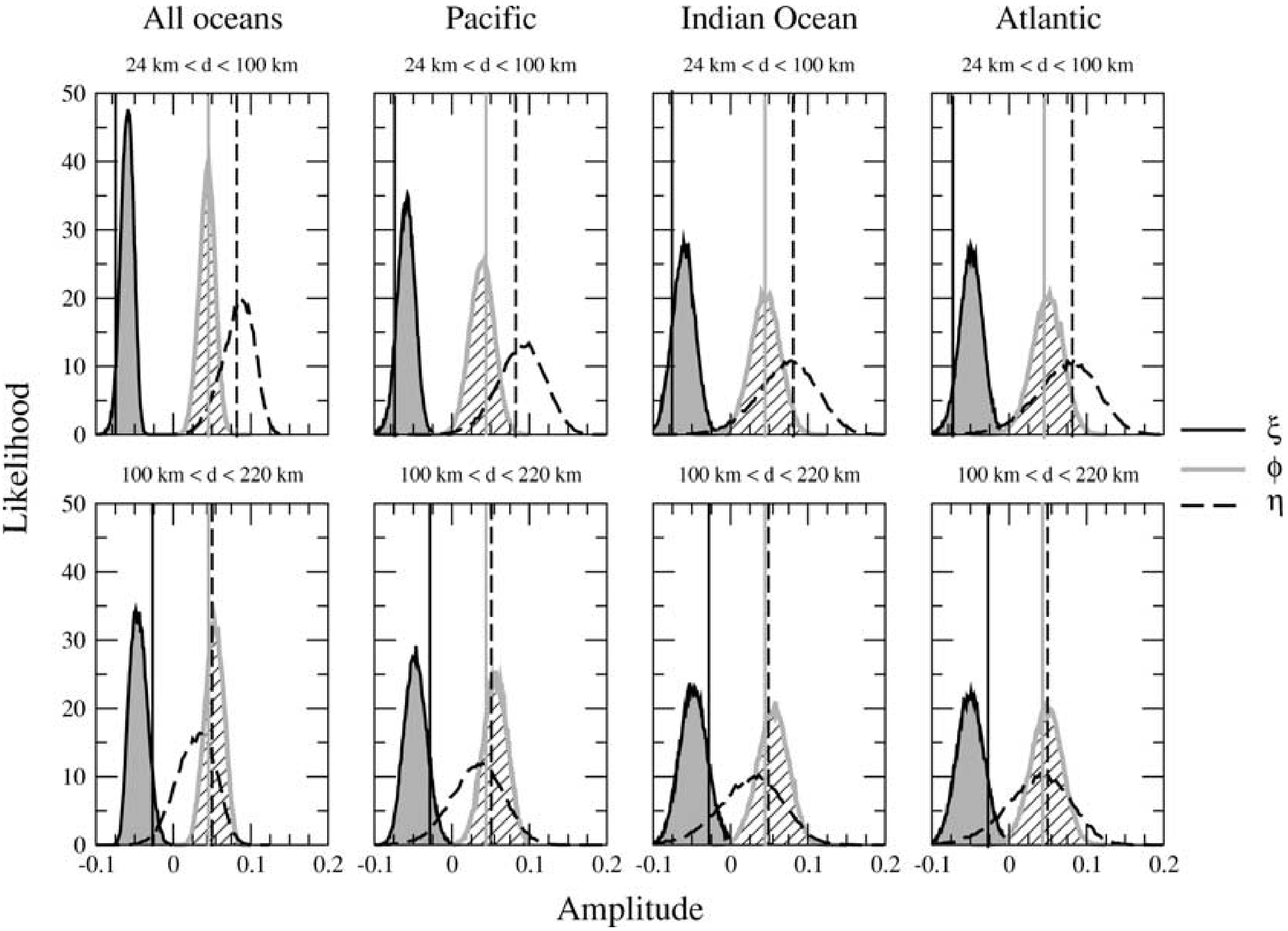

Figure 1. Likelihood of *S*-wave anisotropy (solid black line, grey shading), *P*-wave anisotropy (grey line, stripes) and η anisotropy (dashed line) beneath oceans. The vertical lines indicate the value of ξ, ϕ and η in PREM, averaged over the two layers. The upper and the lower panels have the same vertical and horizontal scales.

computed to determine whether the seismological data employed can put robust constraints on radial anisotropy and density anomalies, under continents and oceans. To analyse the distribution of a parameter δm in an area $\mathcal{A}$, we divided this area into N cells of area $\mathcal{A}_i$ and integrated δm over each cell, for all the models generated:

$$\delta m_i = \int_{\mathrm{cell}i} \delta m(\theta, \phi)\, d\Omega. \tag{10}$$

The δm_i were then added to one another and the resulting sum was divided by the total area $\mathcal{A}$ to get:

$$\overline{\delta m} = \frac{1}{\mathcal{A}} \sum_{i=1}^{N} \delta m_i. \tag{11}$$

Histograms were constructed by accumulating the average $\overline{\delta m}$ obtained for each model. These distributions represent thus the range of data-compatible values of δm, averaged over area $\mathcal{A}$ and do not account for variations within the area considered.

4 RESULTS

Figs 1 to 3 show the distribution of values for parameter ξ, ϕ and η in the two upper layers, obtained by randomly sampling each $\delta m^t{}_s$ according to their PPDFs, reconstructing and averaging the resulting ξ, ϕ or η over a selected region. The histograms have been normalized to 1 to represent PPDFs. The distinction between continents and oceans was made using the 3SMAC model (Nataf & Ricard 1996). From the PPDFs, we computed the probability of having less *S*-wave anisotropy, *P*-wave anisotropy and η-anisotropy (in absolute value) than in PREM in the different areas (Table 1). The vertical lines correspond to the PREM values of ξ, ϕ and η averaged over our layers.

Let us first focus on *S*-wave anisotropy. Fig. 1 displays the PPDFs of the average ξ under the Pacific, the Atlantic and the Indian ocean and under all the oceans combined. The distributions for the Pacific, the Atlantic and the Indian ocean are very similar and their peaks show a very slight decrease of ξ with depth, except maybe under the Atlantic. This rather uniform *S*-wave anisotropy has already been observed by Montagner & Tanimoto (1991). A robust feature also visible is that ξ is smaller than PREM between 24 and 100 km depth and larger than PREM between 100 and 220 km depth. This shows that the variation of *S*-wave anisotropy with depth beneath oceans is not as strong as in the reference model. This characteristic, well resolved by our data, was observed earlier by Ekström & Dziewonski (1998) under the Pacific ocean, but we show that this departure from PREM is typical of other oceans as well.

Model 3SMAC (Nataf & Ricard 1996) allows to distinguish oceans according to their age. Nishimura & Forsyth (1989) observed an increase of ξ with the age of the ocean floor beneath the

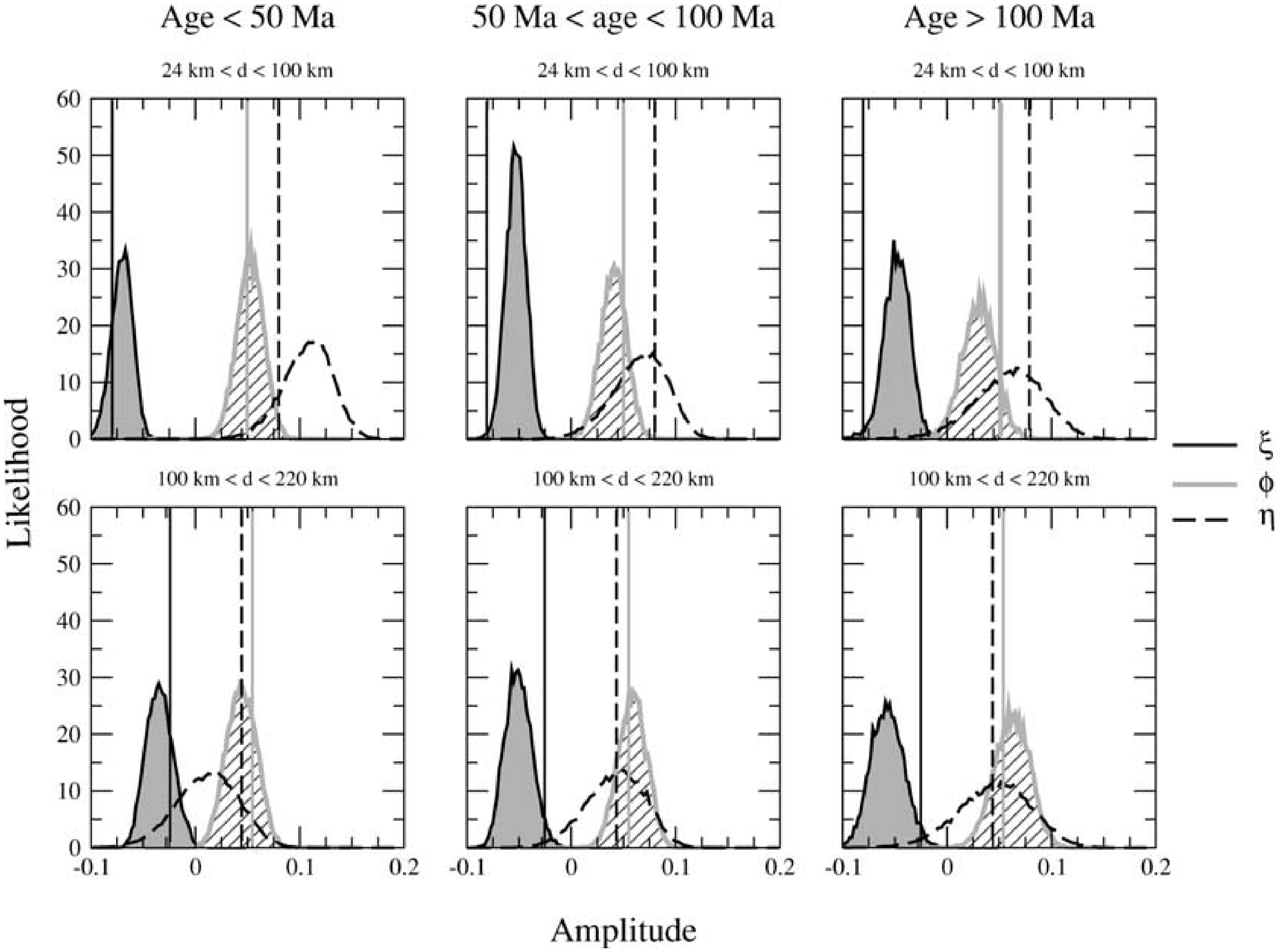

Figure 2. Likelihood of *S*-wave anisotropy (solid black line, grey shading), *P*-wave anisotropy (grey line, stripes) and η anisotropy (dashed line) beneath oceans according to their age. The vertical lines indicate the value of ξ, ϕ and η in PREM, averaged over the two layers. The upper and the lower panels have the same vertical and horizontal scales.

Pacific ocean, with a fast increase in the first 20 Myr until a sort of equilibrium is reached for older regions. Our lateral resolution of degree 8 is not sufficient to make such a precise age distinction. Therefore, we generated histograms of ξ for oceans younger than 50 Myr, for oceans aged between 50 and 100 Myr, and for oceans older than 100 Myr. Inspection of Fig. 2 reveals a clear departure from PREM for ξ beneath oceans older than 50 Myr in the two layers, with a change of sign as observed in Fig. 1. For young oceans the trend is similar, but the deviation from PREM is not as strong as for older oceans. Similar to the study of the Pacific ocean by Montagner (1985), we observe a general increase of the depth extent of shear wave anisotropy with the age of the ocean floor. There is no observable difference between oceans older than 100 Myr and oceans in the age range 50–100 Myr, similar to the flattening observed by Nishimura & Forsyth (1989) beyond 20 Myr. However, if we compare the results for oceans aged between 0 and 50 Myr and older oceans, we do not find an increase of the amplitude of ξ with age at all depths. Our models show a decrease of ξ with age in the top 100 km and an increase deeper. The probability that ξ is smaller than PREM in absolute value is given in Table 1. We find, in the top layer, a probability of 0.84 for oceans younger than 50 Myr and a probability of 0.99 both for oceans aged between 50 and 100 Myr and for oceans older than 100 Myr. The deviation from PREM has thus a slightly smaller probability for young oceans than for older ones. The same is true for the deeper layer.

Fig. 3 displays the values of ξ under continents. No significant deviation in *S*-wave anisotropy from PREM was observed under continents taken as a whole. However, we found a clear age-related signal (see also Table 1). Platforms and tectonically active regions are similar and moderate change relative to PREM is observed. On the contrary, cratons display less *S*-wave anisotropy than the world average in the top 100 km and more anisotropy at depths between 100 and 220 km, like most oceans. The strength of the anisotropy beneath cratons does not change much with depth, similarly to what is observed beneath old oceans. This is very different for younger continental lithosphere where the depth variation is rather strong. *S*-wave anisotropy is therefore most likely the strongest beneath young continents in the top 100 km.

Our data do not have as much sensitivity to *P*-wave related parameters (δC_s^t and δA_s^t) as to *S*-wave related parameters (this is clearly visible on some of the PPDF for the individual SH coefficients, not shown here, which show broad peaks). If the data were to be inverted, the resulting δC and δA models would be highly coupled to each other and to δL and δN by regularization. Using the NA and imposing no explicit regularization in the model space, we found all models compatible with the data, independent of the sensitivity.

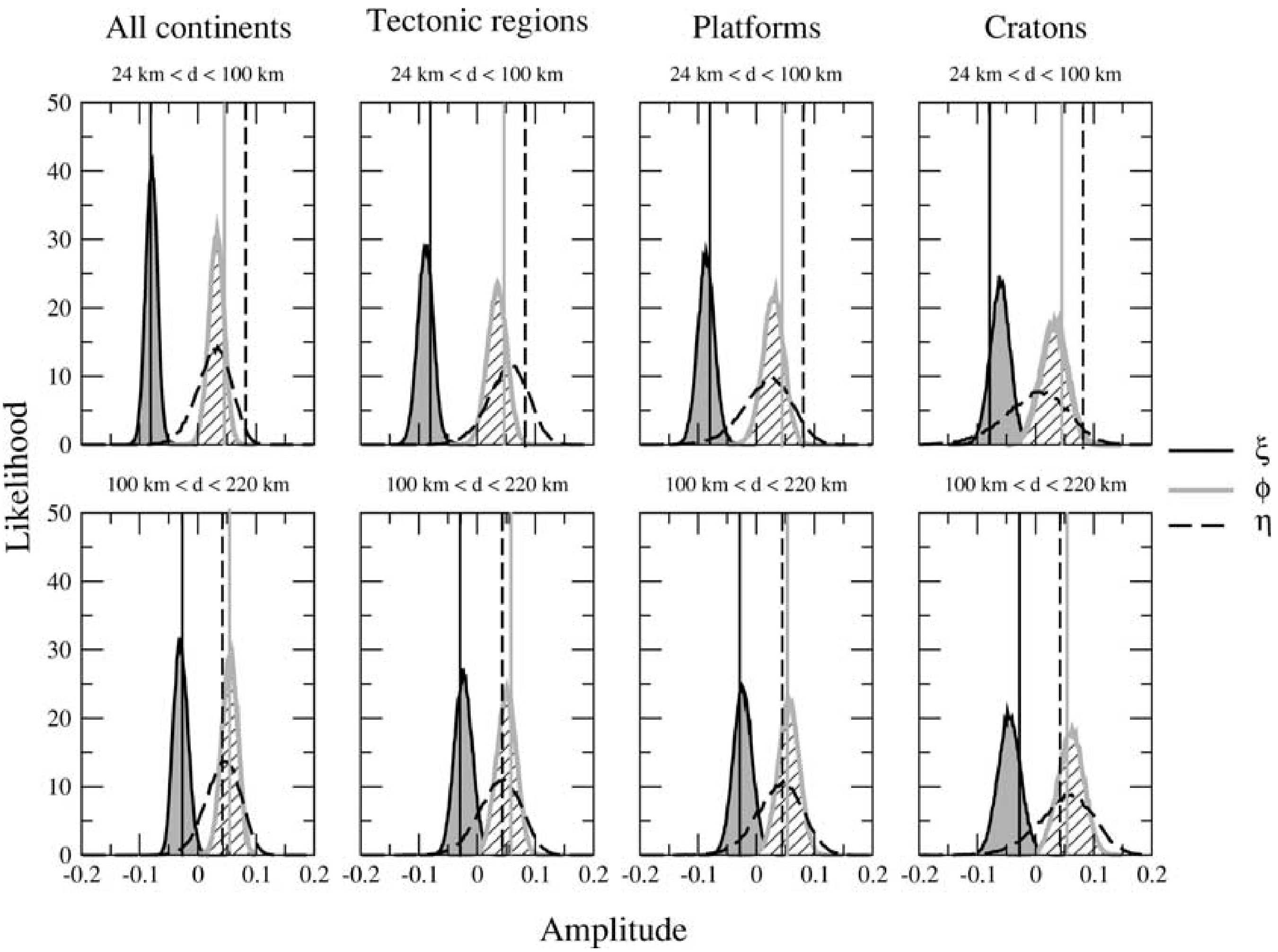

Figure 3. Likelihood of S-wave anisotropy (solid black line, grey shading), P-wave anisotropy (grey line, stripes) and η anisotropy (dashed line) beneath continents. The vertical lines indicate the value of ξ, ϕ and η in PREM, averaged over the two layers. The upper and the lower panels have the same vertical and horizontal scales.

Inspection of the posterior covariance matrix showed, indeed, little trade-offs between parameters with high and small sensitivity, but large values on the diagonal. To show the P-wave anisotropy signal, we computed the overall distribution of ϕ, by randomly resampling the PPDFs associated with each δC_s^t and δA_s^t, as described earlier. Although the PPDFs for ϕ are not much broader than those for ξ, we want to underline that they are obtained by fewer well-resolved SH coefficients than those for ξ. No significant departure from PREM is found for ϕ beneath the various oceans (Fig. 1 and Table 1), but there seems to be a slight age dependence (Fig. 2 and Table 1). In the top 100 km, the deviation from PREM varies from positive values for young oceans towards negative values for older oceans and opposite in the deepest layer. The upper 100 km beneath continents are characterized by a smaller P-wave anisotropy than in PREM (Fig. 3 and Table 1). No clear age related signal is seen.

The PPDFs for parameter η do not show any significant deviation from PREM under oceans as a whole (Fig. 1 and Table 1), but a clear age dependence is visible in Fig. 2 and Table 1. As for ξ, young oceanic lithosphere shows a rapid decrease of η with depth while older oceans are characterized by a more constant η. It is also interesting to notice that, like for S-wave anisotropy, old oceans are most likely characterized by less η anisotropy than young oceans in the top 100 km. The PPDFs of Fig. 3 clearly display less anisotropy than in PREM under continents in the top 100 km (see also Table 1). It is quite likely that cratons do not have any η anisotropy in the uppermost layer [we computed $P(\eta > 0) = 0.52$], and that the level of η anisotropy increases for younger continental lithosphere, similarly to what was observed for oceanic lithosphere. There might be some positive departure from PREM for η beneath cratons in the depth range 100–220 km, but the signal is weak. Elsewhere, PREM gives a good approximation for η.

Montagner & Anderson (1989) investigated the correlations between parameters ϕ, ξ and η for two different petrological models (pyrolite and piclogite). They found a strong correlation between $N/L - 1$ ($-\xi$ in our notation) and η and between $1 - C/A$ (our ϕ) and $N/L - 1$, independent of the two petrological models employed. They proposed to use these correlations to derive scaling factors between $d\xi$, $d\phi$ and $d\eta$, in order to reduce the number of parameters in inversions of seismological data. They also noticed that most seismological models of upper-mantle anisotropy do not fall within their estimates of ξ, ϕ and η, and that there were large regional variations among these models. They proposed that scaling relationships from petrological models should be used as *a priori* constraints in tomographic inversions. Our study provides unbiased and independent constraints on the regional variations of the three parameters ξ, ϕ and η. We computed the overall correlation between $d\xi = \xi - \xi_{\text{prem}}$ and $d\phi = \phi - \phi_{\text{prem}}$, but did not see any significant correlation or anticorrelation (Fig. 4) between the two variables.

Table 1. Probability of having less anisotropy than in PREM (indicated by subscript p).

Area	Depth (km)	$P(\lvert\xi\rvert < \lvert\xi_{\mathrm{p}}\rvert)$	$P(\phi < \phi_{\mathrm{p}})$	$P(\eta < \eta_{\mathrm{p}})$
All oceans	$24 < d < 100$	0.99	0.52	0.46
	$100 < d < 220$	0.06	0.55	0.73
Pacific	$24 < d < 100$	0.96	0.63	0.98
	$100 < d < 220$	0.10	0.45	0.42
Indian ocean	$24 < d < 100$	0.90	0.48	0.93
	$100 < d < 220$	0.13	0.48	0.53
Atlantic	$24 < d < 100$	0.98	0.42	0.78
	$100 < d < 220$	0.09	0.63	0.54
All oceans younger than 50 Myr	$24 < d < 100$	0.69	0.27	0.14
	$100 < d < 220$	0.31	0.81	0.87
All oceans $50 <$ age < 100 Myr	$24 < d < 100$	0.87	0.56	0.70
	$100 < d < 220$	0.18	0.35	0.47
All oceans older than 100 Myr	$24 < d < 100$	0.83	0.74	0.75
	$100 < d < 220$	0.19	0.33	0.45
All continents	$24 < d < 100$	0.49	0.83	0.99
	$100 < d < 220$	0.46	0.50	0.51
All cratons	$24 < d < 100$	0.86	0.73	0.98
	$100 < d < 220$	0.20	0.39	0.42
All platforms	$24 < d < 100$	0.32	0.80	0.93
	$100 < d < 220$	0.61	0.49	0.53
All tectonically active regions	$24 < d < 100$	0.26	0.68	0.78
	$100 < d < 220$	0.61	0.60	0.54

The distributions are centred on zero, which is easily understandable, because either ϕ or ξ shows no deviation from PREM for a given tectonic province. The overall correlation between $d\xi$ and $d\eta = \eta - \eta_{\mathrm{prem}}$ (Fig. 5) is slightly negative (around -0.3) in the two layers. These correlations are indeed small and do not necessarily justify an overall scaling between these parameters. To make a more regional analysis of the behaviour of $d\phi$ relative to $d\xi$, we computed the distribution of their ratios beneath oceans, cratons, platforms and tectonically active regions. Fig. 4 shows the PPDFs for the ratios of the average $d\phi$ over the average $d\xi$ (not the average of $d\phi/d\xi$). The ratio is slightly negative beneath cratons (the peak is situated around -0.5) and slightly positive (around 0.5) beneath platforms and tectonically active regions, in the upper 100 km of the mantle. At larger depths, the distributions are centred on zero. The ratios of the averaged η over the averaged $d\xi$ (Fig. 5) are clearly age related beneath continents in the depth range 24–100 km and suggest more lateral variations in parameter η than in S-wave anisotropy. The ratio is negative beneath cratons in the top layer, with a peak at -2.5. It is positive beneath platforms (around 2) and no significant signal is observed for tectonically active regions and oceans. Between 100 and 220 km depth, the distributions of ratios are more uniform, slightly negative for cratons and centred on zero elsewhere. All distributions are wide, and most commonly used scalings ($-1.5 <= d\phi/d\xi <= -0.5$ and $-2.5 <= d\eta\ /\ d\xi <= -1.75$) fall within our PPDFs. However, if we believe that the seismological data contain information on these parameters and our analysis does not show the contrary, one might be better off neglecting $d\phi$ and $d\eta$ altogether in inversions with the risk of biasing the uppermost mantle beneath continents through η. Our preferred approach would be to use the PPDFs of Figs 4 and 5 together with the method of Montagner & Anderson (1989) to put bounds on regional petrological variations.

Models for the equivalent isotropic perturbations in S- and P-wave velocity ($d\ \ln V_s$ and $d\ \ln V_p$) were randomly generated from the PPDFs of each model parameter, as described earlier. The models obtained for $d\ \ln V_s$ and $d\ \ln V_p$ in the two upper layers are very similar to those usually found: continents are fast and oceans are slow on average and there is a good correlation between S and P anomalies down to 220 km depth. Distributions for the $d\ \ln V_s/d\ \ln V_p$ were also generated (not displayed here) and showed ratios with a peak at $d\ \ln V_s/d\ \ln V_p = 1$, but the distributions are sufficiently large that they cannot be used to discriminate between thermal or compositional effects. Fig. 6 displays PPDF for the variation of $d\ \ln V_s$ with the age of the ocean floor and in different continental regions. There is a clear age dependence in the two top layers beneath oceans and beneath continents. As first observed by Zhang & Tanimoto (1991), while young oceans display slow velocity anomalies, older oceans are characterized by fast velocities. The time variation in the top layer appears to correspond to the $t^{1/2}$ law proposed by Zhang & Tanimoto (1991), where t is the age of the ocean floor, but the age dependence seems more linear at greater depths. Beneath continents, $d\ \ln V_s$ is found to be characterized by cratons faster than platforms, which in turn are faster than active tectonic regions.

A last parameter is density. Most density models were anticorrelated to the velocities and our mean $d\ \ln\rho$ was very similar to the model obtained by Ishii & Tromp (2001) at the corresponding

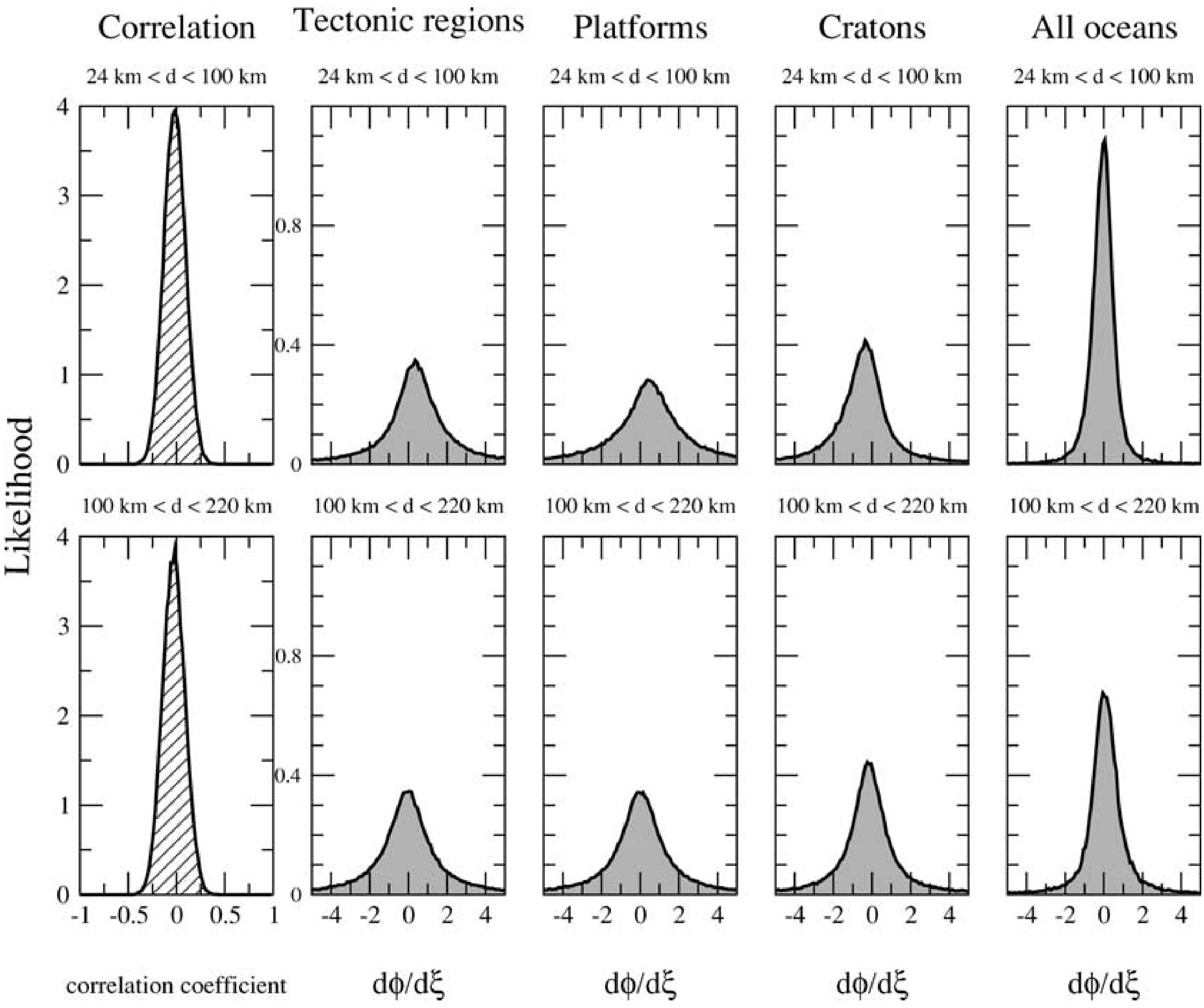

Figure 4. Likelihood of correlation between $d\phi$ and $d\xi$ and likelihood of $d\phi/d\xi$ in various tectonic regions.

depths. While Resovsky & Trampert (2002) demonstrated that NA applied to a data set composed of fundamental and overtone surface waves and normal modes can resolve lateral variations in density anomalies, we tested whether fundamental mode surface waves alone can resolve density. For several SH coefficients, we did not allow any density anomaly (i.e. $\delta\rho_s^t = 0$) and we did not observe any significant change in the other model parameters, the five elastic coefficients. This indicates a low trade-off between elastic coefficients and density anomalies. The low resolution of $\delta\rho$ is clearly visible in the 2-D marginal probability functions that are obtained from the NA. Fig. 7 displays one of these marginals for variables at degree 2 and order zero between 100 and 220 km depth. The region of acceptable values for $d\rho_2^0$ is large, extending both in positive and negative domains, which is evidence for the low resolution of density, compared to the *S*-wave related parameter. The weak peak where $\delta\rho_2^0$ and δN_2^0 have values of opposite signs corresponds to the most likely model, but the 2-D marginal clearly shows that this is not robust. Further, the small tilt of this 2-D marginal confirms a low trade-off between density and the elastic parameter. It clearly demonstrates that, while $\delta\rho$ is not robust, the anisotropic parameters remain unaffected by this undetermination.

5 CONCLUDING REMARKS

The application of the NA to degree 8 fundamental mode Love and Rayleigh wave phase velocity maps allowed us to retrieve robust information on the lateral variations of radial anisotropy in the upper 220 km of the mantle. The method employed is a derivative-free model space search technique, which presents the advantages of not requiring any unnecessary regularization on the model space. The results show that ξ is negative in the two layers down to 220 km, below oceans and below continents, which means that horizontally polarized shear waves travel faster that vertically polarized shear waves ($V_{\mathrm{SH}} > V_{\mathrm{SV}}$).

Cratons can be distinguished from younger continental regions using the depth variation of *S*-wave anisotropy. Our results show that *S*-wave anisotropy is almost constant beneath cratons down to at least 220 km depth, as opposed to platforms and tectonically active regions where a strong decrease of ξ is observed with depth. This could be associated to the depth of continental roots, with a continental lithosphere thicker in old regions than young regions. Our results also suggest that cratons have somewhat less *S*-wave anisotropy than younger continental regions in the top 100 km and

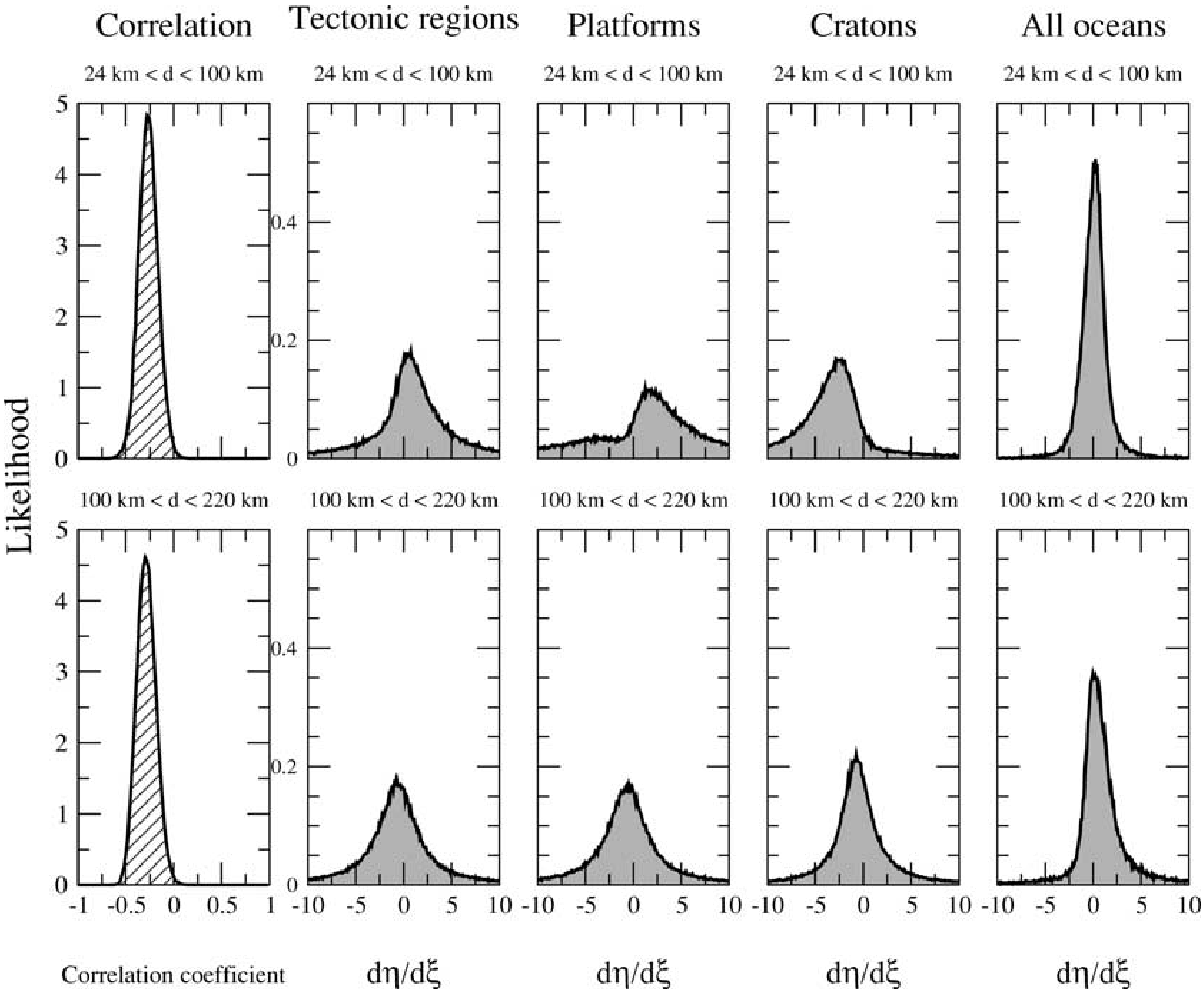

Figure 5. Likelihood of correlation between $d\eta$ and $d\xi$ and likelihood of $d\eta/d\xi$ in various tectonic regions.

the departure from PREM is generally stronger beneath cratons. No significant age dependence is observed within continents for *P*-wave anisotropy. η is most likely zero beneath cratons in the top 100 km and increases for younger continental regions, similarly to ξ. No changes relative to PREM are visible in the deepest layer, both for ϕ and for η.

S-wave anisotropy beneath oceans is rather uniform (no difference is observed from one ocean to another) and similar to the signal for cratons. The data clearly require less *S*-wave anisotropy than in PREM in the top 100 km beneath oceans and cratons, and more anisotropy in the depth range 100–220 km. A strong age-related signal is, however, observed in oceanic lithosphere, similar to the age-dependent signal in continental lithosphere. *S*-wave anisotropy decreases with depth beneath young oceans, while older oceans display less depth variation, suggesting deeper anisotropy and possibly thicker lithosphere in old oceanic regions. From the point of view of *S*-wave anisotropy, this means that cratons and old oceans are much more alike than commonly thought. Young continental and young oceanic lithospheres have a similar depth pattern of *S*-wave anisotropy, within the limits of our layered parametrization. The depth dependence of ξ beneath oceans is compatible with the general observation of Gung *et al.* (2003) of $V_{\mathrm{SH}} > V_{\mathrm{SV}}$ between 80 and 200 km depth under ocean basins and down to at least 200 km depth under cratons. Parameter η follows a similar age dependence as ξ within oceans, with less anisotropy beneath old oceanic lithospheres than beneath younger ones in the top 100 km. The trend is reversed between 100 and 220 km depth.

P-wave anisotropy shows little deviation from PREM and η differs from PREM only in the first 100 km. With the NA, we have been able to retrieve valuable information on these two parameters that is lost in traditional inversions. To underline this point, the correlations and ratios between $d\phi$ and $d\xi$ and between $d\eta$ and $d\xi$ were computed for different regions to test the assumption of proportionality between these variables commonly used in inversions. Our results showed that fundamental mode surface wave data do not favour any particular ratio between perturbations in *P*-wave and *S*-wave anisotropy. The ratio $d\eta/d\xi$ is highly dependent on the regions considered. It is different for oceans and for continents and it is clearly age related within continents. This information should be used to constrain the mineralogy regionally, rather than prescribe global proportionality factors in inversions.

The equivalent isotropic shear wave velocity varies with age of the continental region considered in the two layers, older regions being faster than young ones. We also observe an age variation of

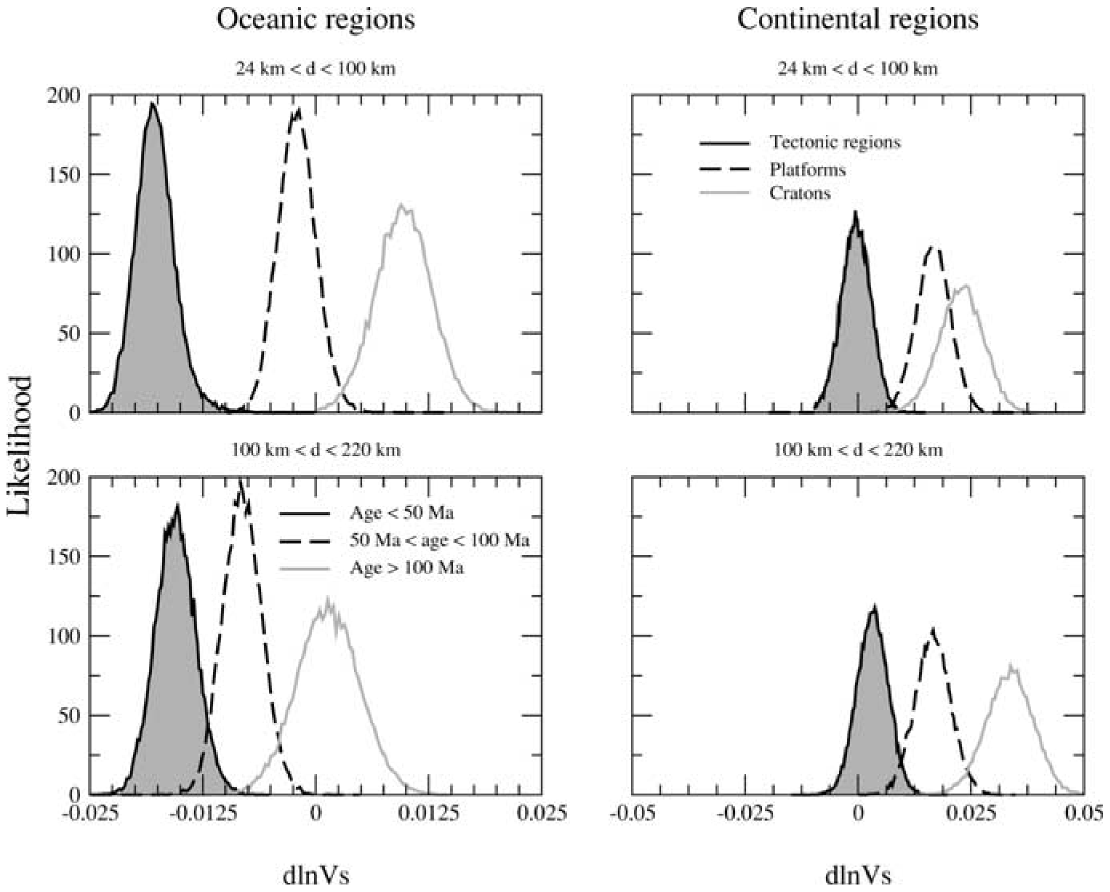

Figure 6. Likelihood of $d \ln V_s$ in the top layers for oceans according to the age of the ocean floor and for different continental regions.

$d \ \ln V_s$ in the upper 100 km of the oceans that could correspond to the $a + bt^{1/2}$ law proposed by Zhang & Tanimoto (1991), but we do not have enough points to confidently estimate a and b. A more linear age-related signal is observed at greater depths. These observations for $d \ \ln V_s$ in the oceans are compatible with a thickening of oceanic lithosphere with age, more rapid for young oceans than older ones. Parameter ξ could, therefore, characterize the depth extent of the oceanic lithosphere, although the rough parametrization we adopted does not allow us to make a precise interpretation of our results in terms of lithosphere–asthenosphere.

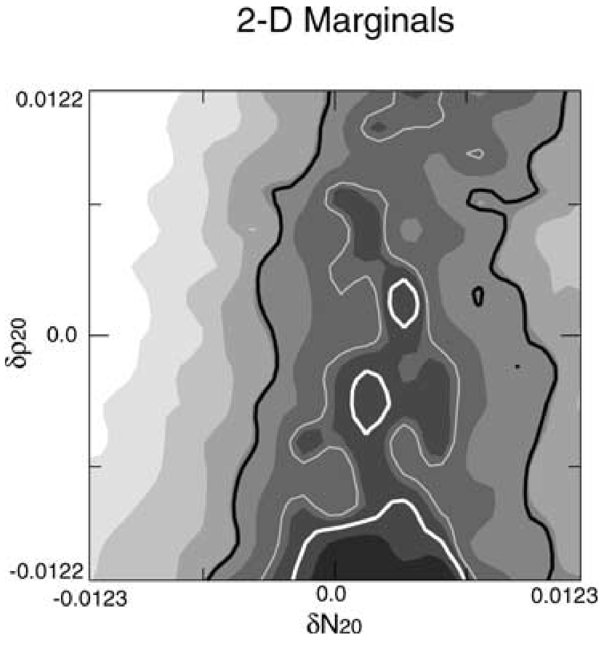

Figure 7. 2-D marginal for $\delta\rho_{20}$ and δN_{20} between 100 and 220 km depth. The thick white line represents the 10 per cent confidence level, grey line corresponds to the 30 per cent confidence level and the thick black line is the 70 per cent confidence level. The range on the horizontal scale corresponds goes from -5 to $+5$ per cent of the value of parameter N in PREM and the range on the vertical scale goes from -2 to $+2$ per cent of the value of ρ in PREM.

ACKNOWLEDGMENTS

The authors are grateful to M. Sambridge for making his Neighbourhood Algorithm available and maintaining a well-documented web site.

REFERENCES

Anderson, D.L., 1961. Elastic wave propagation in layered anisotropic media, *J. geophys. Res.,* **66,** 2953–2963.

Beghein, C. & Trampert, J., 2003. Robust normal mode constraints on inner-core anisotropy from model space search, *Science,* **299,** 552–555.

Beghein, C., Resovsky, J. & Trampert, J., 2002. P and S tomography using normal mode and surface wave data with a neighbourhood algorithm, *Geophys. J. Int.,* **149,** 646–658.

Cara, M., Nercessian, A. & Nolet, G., 1980. New inferences from higher mode data in western Europe and northern Eurasia, *Geophys. J. R. astr. Soc.,* **61,** 459–478.

Dahlen, F.A. & Tromp, J., 1998. *Theoretical Global Seismology,* Princeton Univ. Press, Princeton, NJ.

Debayle, E. & Kennett, B.L.N., 2000. Anisotropy in the Australasian upper mantle from Love and Rayleigh waveform inversion, *Earth planet. Sci. Lett.,* **184,** 339–351.

Dziewonski, A.M. & Anderson, D.L., 1981. Preliminary reference Earth model, *Phys. Earth planet. Int.,* **25,** 25 297–25 356.

Edmonds, A.R., 1960. *Angular Momentum and Quantum mechanics*, Princeton Univ. Press, Princeton, NJ.

Ekström, G. & Dziewonski, A.M., 1998. The unique anisotropy of the Pacific upper mantle, *Nature,* **394,** 168–172.

Ekström, G., Tromp, J. & Larson, E.W.F., 1997. Measurements and global models of surface wave propagation, *J. geophys. Res.,* **102,** 8137–8157.

Forsyth, D.W., 1975. The early structural evolution and anisotropy of the oceanic upper mantle, *Geophys. J. R. astr. Soc.,* **43,** 103–162.

Gaherty, J.B. & Jordan, T.H., 1995. Lehmann discontinuity as the base of an anisotropic layer beneath continents, *Science,* **268,** 1468–1471.

Gung, Y., Panning, M. & Romanowicz, B., 2003. Global anisotropic and the thickness of continents, *Nature,* **422,** 707–711.

Hadiouche, O., Jobert, N. & Montagner, J.-P., 1989. Anisotropy of the African continent inferred from surface waves, *Phys. Earth planet. Int.,* **58,** 61–81.

Hess, H., 1964. Seismic anisotropy of the uppermost mantle mantle under the oceans, *Nature,* **203,** 629–631.

Ishii, M. & Tromp, J., 2001. Even-degree lateral variations in the Earth's mantle constrained by free oscillations and the free-air gravity anomaly, *Geophys. J. Int.,* **145,** 77–96.

Laske, G. & Masters, G., 1996. Constraints on global phase velocity maps from long-period polarization data, *J. geophys. Res.,* **101,** 16 059–16 075.

Lévêque, J.-J. & Cara, M., 1983. Long-period Love wave overtone data in North America and the Pacific Ocean: new evidence for upper mantle anisotropy, *Phys. Earth planet. Int.,* **33,** 164–179.

Lévêque, J.-J., Debayle, E. & Maupin, V., 1998. Anisotropy in the Indian Ocean upper mantle from Rayleigh- and Love-waveform inversion, *Geophys. J. Int.,* **133,** 529–540.

Love, A.E.H., 1927. *A Treatise on the Theory of Elasticity,* Cambridge Univ. Press, Cambridge.

Mochizuki, E., 1986. The free oscillations of an anisotropic and heterogeneous Earth, *Geophys. J. R. astr. Soc.,* **86,** 167–176.

Montagner, J.-P., 1985. Seismic anisotropy of the Pacific Ocean inferred from long-period surface waves dispersion, *Phys. Earth planet. Int.,* **38,** 28–50.

Montagner, J.-P., 2002. Upper mantle low anisotropy channels below the Pacific Plate, *Earth planet. Sci. Lett.,* **202,** 263–274.

Montagner, J.-P. & Anderson, D.L., 1989. Petrological constraints on seismic anisotropy, *Phys. Earth planet. Int.,* **54,** 82–105.

Montagner, J.-P. & Nataf, B.L.N., 1988. Vectorial tomography—I. Theory, *J. geophys. Res.,* **94,** 295–307.

Montagner, J.-P. & Tanimoto, T., 1991. Global upper mantle tomography of seismic velocities and anisotropies, *J. geophys. Res.,* **96**(B12), 20 337–20 351.

Mooney, W., Laske, G. & Masters, G., 1998. Crust 5.1: a global crustal model at 5 deg × 5 deg, *J. geophys. Res.,* **103**(B1), 727–747.

Nataf, H.-C. & Ricard, Y., 1996. 3SMAC: an a priori tomographic model of the upper mantle based on geophysical modeling, *Phys. Earth planet. Int.,* **95,** 101–122.

Nataf, H.-C., Nakanishi, I. & Anderson, D.L., 1984. Anisotropy and shear-velocity heterogeneities in the upper mantle, *Geophys. Res. Lett.,* **11**(2), 109–112.

Nataf, H.-C., Nakanishi, I. & Anderson, D.L., 1986. Measurements of mantle wave velocities and inversion for lateral heterogeneities and anisotropy 3. Inversion, *J. geophys. Res.,* **91**(B7), 7261–7307.

Nishimura, C.E. & Forsyth, D.W., 1989. The anisotropic structure of the upper mantle in the pacific, *Geophys. J.,* **96,** 203–229.

Resovsky, J.S. & Ritzwoller, M., 1998. New and refined constraints on three-dimensional Earth structure from normal modes below 3 mHz, *J. geophys. Res.,* **103**(B1), 783–810.

Resovsky, J.S. & Trampert, J., 2002. Reliable mantle density error bars: An application of the Neighbourhood Algorithm to normal mode and surface wave data, *Geophys. J. Int.,* **150,** 665–672.

Resovsky, J.S. & Trampert, J., 2003. Using probabilistic seismic tomography to test mantle velocity-density relationships, *Earth planet. Sci. Lett.,* **215,** 121–134.

Sambridge, M., 1999a. Geophysical inversion with a neighbourhood algorithm-I. Searching a parameter space, *Geophys. J. Int.,* **138,** 479–494.

Sambridge, M., 1999b. Geophysical inversion with a neighbourhood algorithm-II. Appraising the ensemble, *Geophys. J. Int.,* **138,** 727–746.

Silveira, G. & Stutzmann, E., 2002. Anisotropic tomographic of the Atlantic Ocean, *Phys. Earth planet. Int.,* **132,** 237–248.

Silver, P.G. & Chan, W.W., 1991. Shear wave splitting and subcontinental mantle deformation, *J. geophys. Res.,* **96,** 16 419–16 454.

Tanimoto, T., 1986. Free oscillations of a slightly anisotropic Earth, *Geophys. J. R. astr. Soc.,* **87,** 493–517.

Tanimoto, T. & Anderson, D.L., 1984. Mapping convection in the mantle, *Geophys. Res. Lett.,* **11**(4), 287–290.

Tarantola, A., 1987. *Inverse Problem Theory, Methods for Data Fitting and Model Parameter Estimation,* Elsevier, Amsterdam.

Trampert, J., 1998. Global seismic tomography: the inverse problem and beyond, *Inverse Problems,* **14,** 371–385.

Trampert, J. & Woodhouse, J.H., 1995. Global phase velocity maps of Love and Rayleigh waves between 40 and 150 seconds, *Geophys. J. Int.,* **122,** 675–690.

Trampert, J. & Woodhouse, J.H., 1996. High resolution global phase velocity distributions, *Geophys. Res. Lett.,* **23,** 21–24.

Trampert, J. & Woodhouse, J.H., 2001. Assessment of global phase velocity models, *Geophys. J. Int.,* **144,** 165–174.

Trampert, J. & Woodhouse, J.H., 2003. Global anisotropic phase velocity maps for fundamental mode surface waves between 40 and 150 seconds, *Geophys. J. Int.,* **154,** 154–165.

van Heijst, H.J. & Woodhouse, J.H., 1999. Global high-resolution phase velocity distributions of overtone and fundamental-mode surface waves determined by mode branch-stripping, *Geophys. J. Int.,* **137,** 601–620.

Wong, Y.K., 1989. Upper mantle heterogeneity from phase and amplitude data of mantle waves, *PhD thesis*, Harvard Univ., Cambridge, MA.

Zhang, Y.-S. & Tanimoto, T., 1991. Global Love wave phase velocity variation and its significance to plate tectonics, *Phys. Earth planet. Int.,* **66,** 160–202.